



Article

Microwave Common-Frequency Absorption/Transmission Mode Conversion Based on Active Components

Yisen Luo ¹, Wenning Wang ², Chong-Zhi Han ^{3,*}  and Tongyu Ding ^{3,*} 

¹ College of Computer and Information Engineering, Henan Normal University, Xinxiang 453007, China; lysuni@163.com

² Aerospace Changping Technology Co., Ltd., Beijing 100080, China; wangwenning@empchina.cn

³ School of Ocean Information Engineering, Jimei University, Xiamen 361021, China

* Correspondence: chongzhi_han@foxmail.com (C.-Z.H.); tyding@jmu.edu.cn (T.D.)

Abstract: To overcome the limitations of traditional frequency selective surfaces in flexible state switching at the same frequency, this paper proposes a novel active frequency selective surface (AFSS) that simultaneously exhibits conversion between absorption and transmission modes at the same frequency band. By welding PIN diodes on the bottom structure of the AFSS, the conversion between band-pass (transmission) and band-stop (absorption) filters can be controlled electronically. In the common-frequency switch between absorption and transmission modes, the impedance matching of the AFSS is attained by altering the capacitance value of the varactors embedded on the top structure of the AFSS. The functionalities of the proposed AFSS design are investigated by full-wave simulations (in HFSS software) at 11.4 GHz. Furthermore, the operating principle is analyzed using an equivalent circuit model (in AWR software). To verify the concept, a prototype is manufactured, and the responses of mode switching are measured by adjusting the bias voltage. The measurement result is consistent with the simulation analysis. Owing to the tunability of the varactors, the structural asymmetry is compensated to achieve 80% absorptivity and transmissivity within a field of view of $\pm 35^\circ$. The developed AFSS structure is highly valuable to be used in scenarios such as antenna domes, etc.

Keywords: active frequency selective surface; mode conversion; transmission mode; absorption mode; microwave



Citation: Luo, Y.; Wang, W.; Han, C.-Z.; Ding, T. Microwave Common-Frequency Absorption/Transmission Mode Conversion Based on Active Components. *Electronics* **2023**, *12*, 2876. <https://doi.org/10.3390/electronics12132876>

Academic Editor: Dimitra I. Kaklamani

Received: 21 May 2023

Revised: 25 June 2023

Accepted: 27 June 2023

Published: 29 June 2023



Copyright: © 2023 by the authors. Licensee MDPI, Basel, Switzerland. This article is an open access article distributed under the terms and conditions of the Creative Commons Attribution (CC BY) license (<https://creativecommons.org/licenses/by/4.0/>).

1. Introduction

Since frequency selective surfaces (FSSs) have been developed for use as microwave and millimeter-wave absorbers, they have been widely utilized in stealth, radar cross-section (RCS) reduction, and other systems [1–7]. Considering the complexity and variability of practical application scenarios, the surface impedance of an active frequency selective surface (AFSS) structure can be tailored by introducing tunable components such as graphene [8,9], liquid crystals [10–12], and diodes [13,14], realizing multifunctional AFSSs with tunable absorption, reflection, and transmission.

The traditional AFSS geometry structure comprises periodic metallic patterns printed on opposite sides of a dielectric substrate. They usually use metal as the underlying layer of a multilayer to achieve tunable absorbers. For example, Refs. [15–17] implemented tunable AFSSs with adjustable absorbing frequency, bandwidth, or absorption rate by changing the surface impedance of the top layer of a multilayer. Refs. [18,19] realized wideband multifunction converters for absorption and reflection. However, using metal as the bottom layer of a multilayer will limit the transmission of electromagnetic waves, resulting in the failure of the AFSSs for realizing the dynamic conversion between absorption and transmission modes [20–23].

To solve the above problems, the bottom layer of a multilayer achieved the conversion between band-pass and band-stop filter. Ref. [24] presented an AFSS that realizes a functional switch among absorption, transmission, and total reflection by controlling the

response of the active devices. A tunable AFSS that can switch between absorption and transmission by altering adjustable elements of the top layer of a multilayer was proposed in [25]. Nevertheless, the transmission band is different from the absorption band in the previous study, which not only wastes the spectrum resources but also fails to meet the switch between stealth and communication states. On the other hand, propagation mode control via metasurfaces has also been well documented in recent years, and it is capable of converting a linearly polarized (LP) incident wave into a circularly polarized (CP) wave or its cross-polarized LP wave at different frequencies [26]. Various types of metamaterials with strong electromagnetic resonance have been reported [27–32], for instance, Pan et al. proposed dual-band multifunctional coding metasurface in compact 5G/6G communication systems [27]. This research covered the K band to THz.

In fact, most of the proposed designs realize dynamic switching among absorption, reflection, and transmission by controlling the surface impedance of the structure [33,34]. When the surface impedance of the structure is changed, the resonant frequency will also become different. By shifting the resonant frequency, the mode conversion between absorption/reflection and transmission/reflection can be realized in the same frequency band. However, for the AFSSs with absorbing and transmitting mode conversion, the surface impedances of both the top and bottom layers are changed, which makes it difficult to achieve dynamic switching at the same frequency. Therefore, the goal of this work is to achieve a functional switch between transmission and absorption in the same frequency band.

In this paper, a compact AFSS that can switch between absorption and transmission modes in the same frequency is presented by controlling the lumped components on the AFSS. Its geometry comprises two tunable electric resonators spaced by a dielectric substrate, with varactor and PIN diodes embedded on the top and bottom metallic layers, respectively. The proposed AFSS is fabricated and demonstrated. The numerical and experimental results show that the presented structure has the capability to achieve transmission/absorption conversion in the same frequency of around 11.4 GHz under normal incidence. And the absorption and transmission modes are angularly stable up to 35° by changing the capacitance of the varactors, which compensates for the asymmetry of the structure.

This paper is organized as follows. Section 2 presents the proposed AFSS and corresponding equivalent circuit models based on transmission-line theory. Sections 3 and 4 validate the functionalities of the proposed AFSS in full-wave simulations and experimental measurements, respectively. Finally, Section 5 provides the conclusions, along with a discussion of the potential applications of the proposed AFSS.

2. Design and Analysis

2.1. Design Principle

A compact AFSS that can switch between absorption and transmission modes in the same frequency is presented in this section. The conceptual configuration of the proposed AFSS is shown in Figure 1. When the PIN diodes are in the OFF-state and the varactors are supplied with reverse bias voltage, the AFSS is designed to be transmissive at normal incidence, as illustrated in the right side of Figure 1. Inversely, when the PIN diodes are in the ON-state, the AFSS functions as an absorber, as shown in the left side of Figure 1. In the design, the functions of the top layer varactors are as follows: (1) tuning the capacitance value of varactors and the ON-/OFF-states of PIN diodes achieves the dual-functional switch in the same frequency; and, (2) by adjusting the capacitance value of the varactors, the asymmetry of the structure is compensated, and the dual-functional switching is angularly stable up to 35°.

In this design, the bias network that provides bias voltage for varactors and PIN diodes is embedded into the top and bottom layers, which greatly reduces the manufacturing cost and difficulty [35]. The basic geometry of the designed AFSS is illustrated in Figure 2a,b. The varactors are welded on the top layer, and the PIN diodes are embedded on the bottom

layer of the AFSS. The intermediate layer is a 1 mm thick FR4 substrate (with relative permittivity of $\epsilon = 4.4$ and tangential loss of $\tan \delta = 0.002$). The unit cells are arranged periodically with a period p and printed in copper with a conductivity of $\sigma = 5.8 \times 10^7$ s/m and a thickness of 0.035 mm.

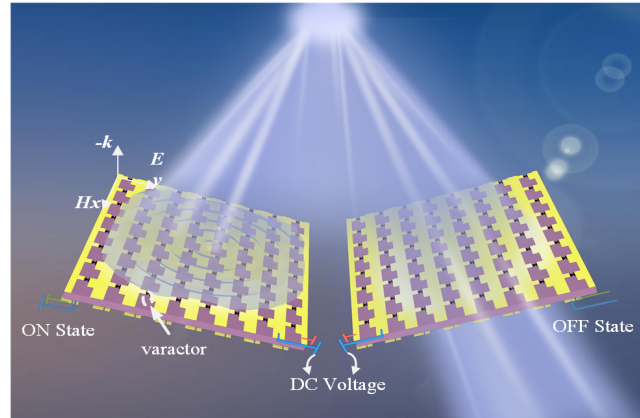


Figure 1. Conceptual configuration of the proposed AFSS with functional switching between absorption and transmission.

The actual current flows through the diodes of the top and bottom layers, as shown in Figure 2c. The diodes are connected in parallel periodically, which means that a small amount of voltage is enough to simultaneously regulate all the lumped elements in a large prototype. In practice, the top and bottom layer diodes are welded in different ways. For a set of adjacent cells on the top layer, varactors are installed so that the cathodes of adjacent units are face to face. Instead, the anodes of adjacent units are opposite to each other. The adjacent PIN diodes on the bottom layer are installed in similar way, with the cathodes facing each other in each cell.

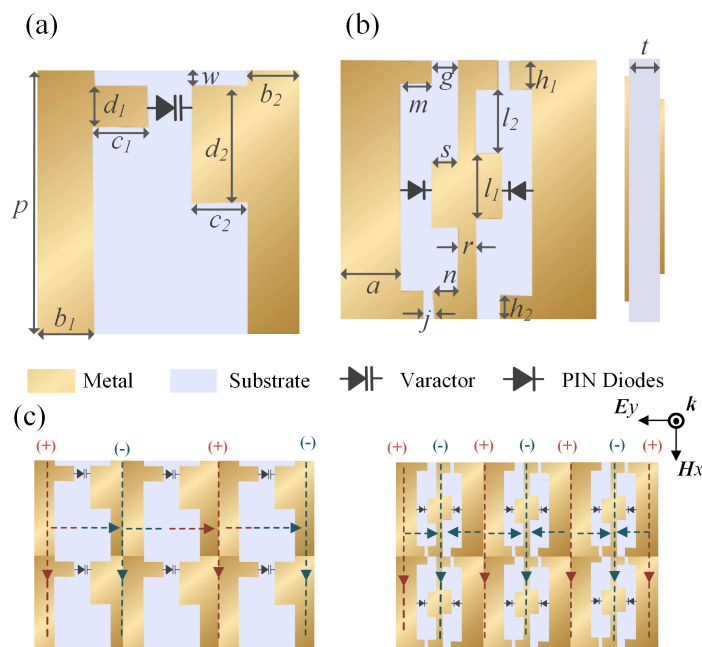


Figure 2. Schematic of the unit cell and biasing network of the proposed integrated absorption–transmission structure: (a) Top view of the designed AFSS; (b) bottom view of the designed AFSS; and (c) biasing voltage network of the designed AFSS. The optimal geometrical dimensions of the proposed AFSS are $p = 9$ mm, $w = 0.57$ mm, $b_1 = c_2 = 1.9$ mm, $b_2 = c_1 = 1.8$ mm, $d_1 = 1.4$ mm, $d_2 = 3.9$ mm, $g = 0.92$ mm, $a = 2.2$ mm, $j = 0.4$ mm, $m = 1.08$ mm, $n = 0.8$ mm, $s = 0.9$ mm, $r = 0.6$ mm, $h_1 = 0.8$ mm, $h_2 = 1$ mm, $l_1 = 2.29$ mm, and $l_2 = 2.21$ mm.

2.2. Equivalent Circuit Analysis

According to the transmission-line theory [36,37], the electromagnetic responses of the designed AFSS with common-frequency conversion between absorption and transmission modes can also be analyzed through an equivalent circuit model. The ON-/OFF-state of the PIN diodes embedded in the bottom layer is equivalent to different circuit models. The corresponding varactors welded on the top layer can be equivalent to a series of resistance, capacitance, and inductance. Figure 3a,b illustrate the equivalent circuit model of the proposed AFSS under the PIN diodes' ON- and OFF-states, respectively. The equivalent circuits of AFSS are obtained using AWR Microwave Office software. The subscripts "t" and "r" correspond to the lumped components on the top and bottom layers, respectively. For the absorption state, C_{t1} and C_{b1} represent the gap capacitances, L_{t2} , C_{t2} , and R_{t2} signify variable lumped components for the varactors. L_{t1} and L_{b1} portray the strip inductances. R_{t1} and R_{b1} are attributed to the resistances of the metal and lossy substrate. The PIN diodes in the ON-state (16 V bias voltage applied) can be represented by a series of resistance (R_{bON}) and inductance (L_{b2}). Accordingly, the OFF-state (5 V bias voltage applied) denotes the parallels of capacitance and resistance. The capacitance is derived from the varactors, while the inductance and resistance are mainly originated from the metallic patterns.

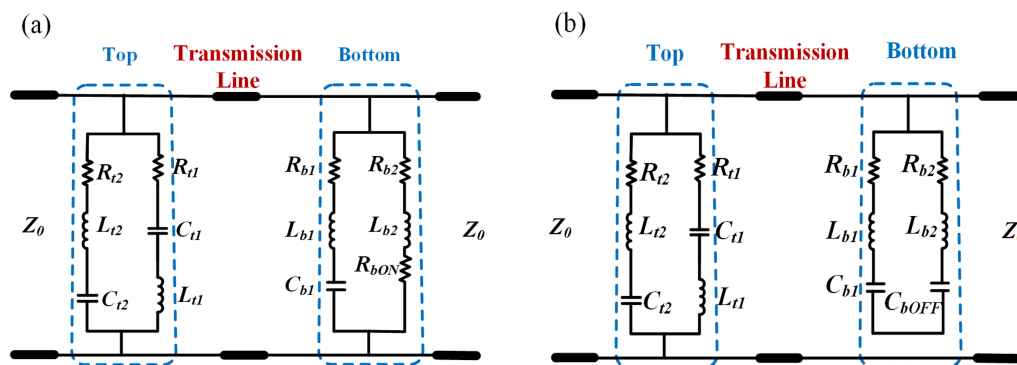


Figure 3. Equivalent circuit model of the proposed AFSSs: (a) equivalent circuit of the diodes in the ON-state; (b) equivalent circuit of the diodes in the OFF-state.

To better understand the working principle from the equivalent circuit models, the impedance of the top and bottom layers can be written as

$$Z_T = (R_{t1} + j\omega L_{t1} + 1/j\omega C_{t1}) \parallel (R_{t2} + j\omega L_{t2} + 1/j\omega C_{t2}) \tag{1}$$

$$Z_B = (R_{b1} + j\omega L_{b1} + 1/j\omega C_{b1}) \parallel (Z_{PIN}) \tag{2}$$

where $Z_{PIN} = R_{b2} + j\omega L_{b2} + R_{ON}$ (ON-state) and $Z_{PIN} = R_{b2} + R_{b2} + 1/j\omega C_{OFF}$ (OFF-state).

Now, the overall impedance of the proposed AFSS can be expressed as

$$Z_{net} = Z_R \parallel Z'_B \tag{3}$$

where Z'_B can be found from the transmission-line theory

$$Z'_B = Z_S \frac{Z_B + jZ_S \tan \theta}{Z_S + jZ_B \tan \theta} \tag{4}$$

where $\theta = \beta t$, with $\beta = 2\pi/\lambda$ being the phase shift constant.

Regarding this model as a two-port network, the equivalent ABCD matrix can be derived as follow [38]:

$$\begin{bmatrix} A & B \\ C & D \end{bmatrix} = \begin{bmatrix} 1 & 0 \\ Y_T & 1 \end{bmatrix} \begin{bmatrix} \cos \theta & jZ_s \sin \theta \\ jY_B \sin \theta & \cos \theta \end{bmatrix} \begin{bmatrix} 1 & 0 \\ Y_B & 0 \end{bmatrix} \quad (5)$$

$$= \begin{bmatrix} \cos \theta + jZ_s \sin \theta & jZ_s \sin \theta \\ (Y_T + Y_B) \cos \theta + j(Y_S + Z_S Y_T Y_B) \sin \theta & jY_B Z_S \sin \theta + \cos \theta \end{bmatrix}$$

By simulating the equivalent circuit model of the above topological structure, the correctness of the proposed equivalent circuit is verified. The scattering results of the equivalent circuit model were acquired by ANSYS HFSS software and the AWR Microwave Office software. Figure 4a,b illustrate the scattering parameters' comparison results between the full-wave simulation and the equivalent circuit model simulation in the transmission and absorption states. To clarify, we described the reflectivity and transmissivity as S_{11} and S_{21} , respectively, because it is sufficient to verify the validity of the AWR software. The solid line represents the full-wave simulation results and the dashed line describes the equivalent circuit simulation results. The proposed equivalent circuit model provides a close agreement between the calculated and full-wave-simulated scattering parameters. Additionally, the corresponding optimized values of the designed structure are listed in Tables 1 and 2, representing the absorption and transmission states, respectively.

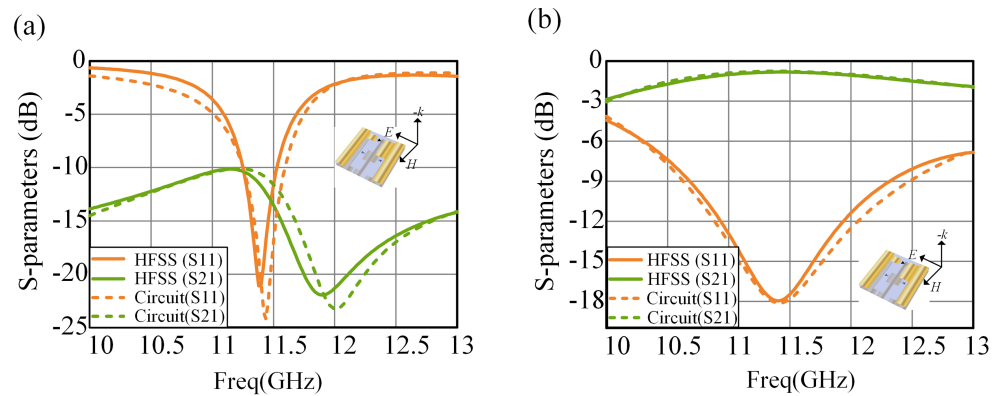


Figure 4. The simulation results comparison in HFSS and AWR: (a) simulated scattering parameters of absorption state; (b) simulated scattering parameters of transmission state.

Table 1. Variable Value of Absorption State.

Variable Symbol	R_{t1}	L_{t1}	C_{t1}	R_{t2}
Variable Value	7.65 ohm	3.42 nH	0.051 pF	35.96 ohm
Variable Symbol	L_{t2}	C_{t2}	R_{b1}	C_{b1}
Variable Value	8.41 nH	0.093 pF	2.81 ohm	1.35 pF
Variable Symbol	L_{b1}	R_{b2}	R_{bON}	L_{b1}
Variable Value	0.26 nH	9.29 ohm	19.12 ohm	0.25 nH

Table 2. Variable Value of Transmission State.

Variable Symbol	R_{t1}	L_{t1}	C_{t1}	R_{t2}
Variable Value	11.17 ohm	49.86 nH	2.16 pF	41.61 ohm
Variable Symbol	L_{t2}	C_{t2}	R_{b1}	L_{b1}
Variable Value	11.3 nH	0.036 pF	1.87 ohm	0.147 nH
Variable Symbol	C_{b1}	R_{b2}	C_{bOFF}	L_{b2}
Variable Value	0.37 pF	0.532 ohm	0.46 pF	0.81 nH

2.3. Surface Current Distribution

To further study the absorption and transmission mechanisms of the proposed structure, the surface current distributions of the AFSS in the absorption and transmission states at 11.4 GHz are shown in Figure 5. Figure 5a,b denotes the surface current distributions on the top and bottom layers, where the bottom layer's diodes are in the OFF-state, and their counterparts Figure 5c,d correspond to the ON-state. It is shown that for the top layer in the different states of the diodes, the current directions are similar, yet the current intensity are different. Concerning the transmission state, the current distribution is primarily concentrated in the diodes. However, it is mainly concentrated on the connection for the absorption state, which maximizes the absorption efficiency. Similarly, the bottom layer is in the OFF-state, and the surface current is weak at the edge and concentrated on the slot, while in the ON-state, the middle gap structure generates strong resonance, ensuring excellent absorption performance at 11.4 GHz.

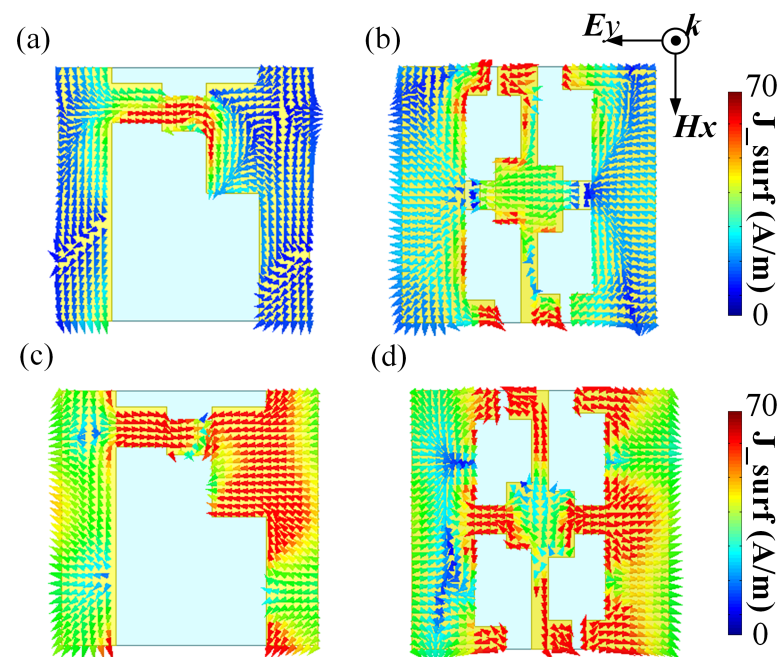


Figure 5. (a,c) are surface current distributions on the top layer of the proposed unit cells for normal incidence at 11.4 GHz for the OFF-state and ON-state, respectively; (b,d) are surface current distributions on the bottom layer of the proposed unit cells for normal incidence at 11.4 GHz for the OFF-state and ON-state, respectively.

3. Numerical Validation and Analysis

Simulation Results

The master–slave boundary condition is set on the side of the model to simulate a plane periodic structure in the simulation. The electromagnetic wave is defined by the Floquet port at normal incidence. The corresponding varactors can be equivalent to an *RLC* circuit with a nonlinear variation. When the bottom layer's diodes are in the ON-state, the underlying geometry demonstrates reflection behavior. By modulating the capacitance value of the varactors to 0.5 pF, the entire AFSS structure satisfies impedance matching, leading to absorbing at around 11.4 GHz (where the insertion loss and return loss are both better than 10 dB), as shown in Figure 6a. The solid line represents the return loss and the dashed line denotes the insertion loss. When the top diodes have 0.8 pF capacitance value and the bottom layer's diodes are in the OFF-state, the overall structure exhibits broadband transmission (with an insertion loss smaller than 1 dB), as illustrated in Figure 6b. It is worth noting that the tunability of the varactors makes it attainable for the topological structure to absorb and transmit in the same frequency band.

The simulation results of the designed AFSS are illustrated in Figure 6a,b, without changing the capacitance value of the varactors under the oblique incidence. By adjusting the capacitance values of the varactors, Figure 6c,d represents that the absorption and transmission modes are angularly stable up to 35°. It is obvious that the varactors embedded in the top layer have a significant effect on compensating the asymmetry of the structure. However, when the incident angle is greater than 35°, for the absorption state, the return loss is distinctly worse than 10 dB at 11.4 GHz, revealing that the structural surface impedance is no longer matched with the free-space wave impedance.

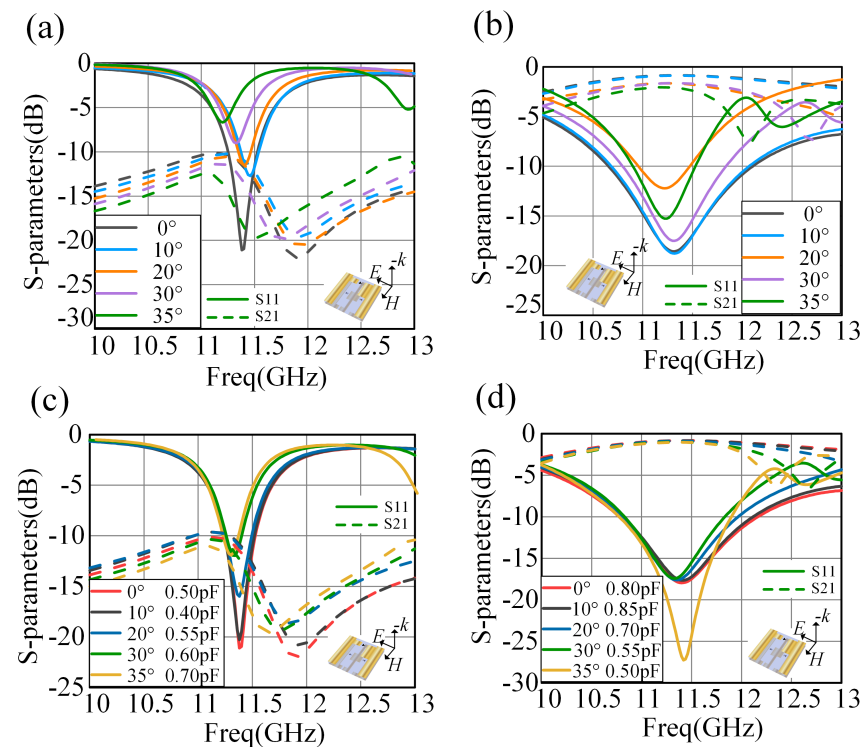


Figure 6. Simulation results at different incident angles in TE polarization of the proposed AFSS: (a) scattering parameters of the absorption state with a 0.5 pF capacitance of the varactors; (b) scattering parameters of the transmission states with a 0.8 pF capacitance of the varactors; and (c,d) are the scattering parameters of the absorption and transmission states by changing the reverse bias voltage of varactors, respectively.

4. Experiment Verification

4.1. Sample Fabrication and Experiment

The proposed AFSS structure was fabricated utilizing printed circuit board (PCB) technology. The top and bottom layers' metal patterns are printed on opposite sides of the 1 mm thick FR4 substrate. PIN diodes (SMP1321-079LF) are embedded on the bottom layer, and varactors (SMV1231-011LF) are mounted on the top layer. Thus, the top and bottom layers' diodes can be adjusted independently by bias voltage network to achieve the switch between absorption and transmission mode at the same frequency. Figure 7a,b are photos of the top and bottom sides of the prototype, respectively. The structure consists of 32×31 units, where the entire size of the sample is 288×279 mm².

For experimental verification [39,40], measurements are carried out in an anechoic chamber. The active components used in this paper are SMP1321-079LF PIN diodes and SMV1231-011LF varactors. A dual DC regulated power supply is used to provide voltage to the diodes. Two X-band standard gain horn antennas are used as transmitting and receiving antennas. The prototype is surrounded by pyramid absorbers to reduce the diffraction effect. Before the measurement, the horn antennas and the prototype should be normalized to eliminate the environmental impact. For transmission measurements,

the two horn antennas are calibrated in free space, and then for reflection tests, a metal plate of the same size as the prototype is used for calibration. Then, the horn antennas are used to transmit the normal incident quasi-plane wave, which is fixed 1 m away from the prototype. The reflection coefficient is measured by placing the transmitting and receiving horn antennas on the same side of the prototype.

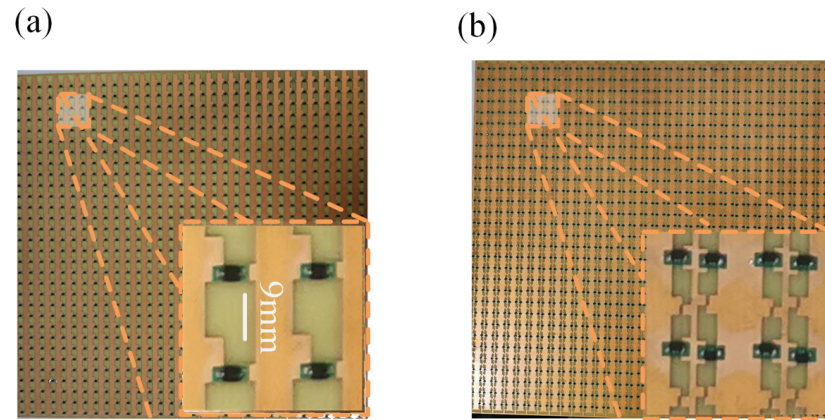


Figure 7. Photograph of the fabricated prototype: (a) top side; (b) bottom side.

4.2. Sample Measurement Results

Based on the above tests, Figure 8a,b illustrate the measurement results of the absorption and transmission states. The experimental results illustrate that when the PIN diodes are in the OFF-state and varactors are loaded with a 5 V bias voltage, the AFSS functions as a bandpass filter at around 11.5 GHz under normal incidence. Accordingly, when the bottom layer's diodes are in the ON-state, the top layer's varactors are loaded with a bias voltage of 16 V, and the AFSS acts as an absorber at around 11.5 GHz. The measurement results have a slight frequency shift compared with the simulation results, and the results of the return loss in the transmission state are higher than the simulation results. This is mainly due to the differences between the active components and the equivalent elements of the diodes' simulation and the manufacturing tolerance of the printed circuit board. Additionally, the dispersion effect of the parasitic elements and the limited size of the manufacturing prototype can also cause deviation between measurement and simulation results, which cannot be ignored.

When an electromagnetic wave is incident on the surface of the medium, the absorptivity and the transmissivity are expressed as

$$A(\omega) = 1 - R(\omega) - T(\omega) = |S_{11}|^2 - |S_{21}|^2 \quad (6)$$

$$T(\omega) = |S_{21}|^2 \quad (7)$$

Considering the TE polarization, the absorptivity and transmissivity are calculated from simulation and measurement, as illustrated in Figure 8c,d, respectively. At around 11.4 GHz, the simulation results show that absorptivity reaches about 92%; meanwhile, the transmissivity is up to 82%. The measurement results illustrate that the absorptivity is 92.5% at 11.5 around GHz, which is consistent with the simulation results, while transmissivity decreased to 78%. The conversion between absorption and transmission modes at 11.5 GHz was achieved by switching the states of the diodes. The absorptivity and transmissivity bandwidth are calculated as 80%, the measured absorption bandwidth is within 11.36–11.83 GHz, and the transmissivity is higher than 70% within 11.15–11.78 GHz. With independent control of the biasing conditions (ON-/OFF-states) of the diodes, the AFSS realizes the same frequency conversion between transmission and absorption modes, unlike the existing articles, as shown in Table 3.

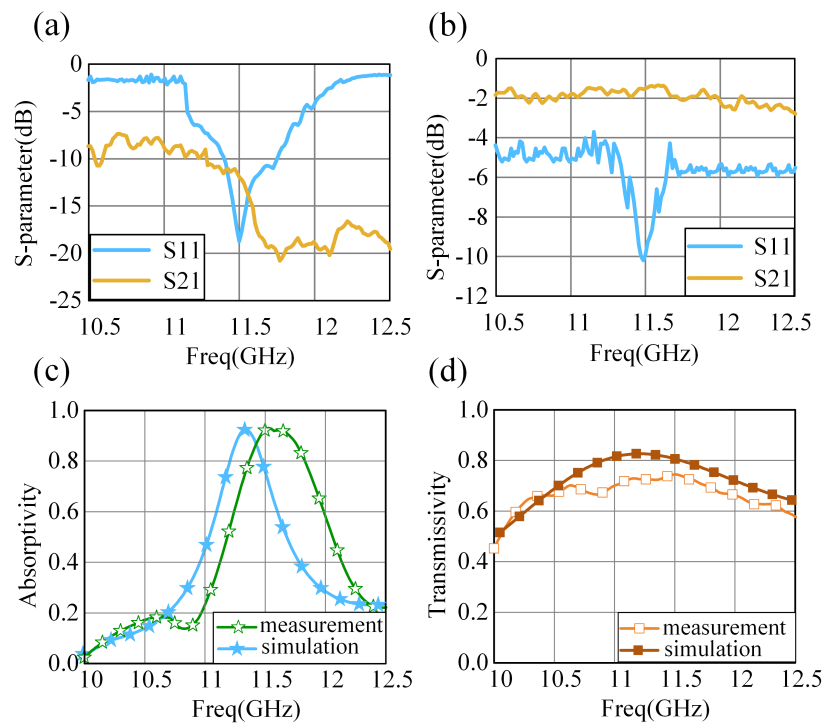


Figure 8. Measurement and simulation results of absorption and transmission modes: (a,b) are the scattering parameters of the measurement absorption and transmission states, respectively; (c,d) show the simulation and measurement absorptivity and transmissivity, respectively.

Table 3. Comparison of this Work with Existing Articles.

AFSS Structure	Working Mode				Biasing Network	Polarization
	Transmission Mode		Absorption Mode			
	Insertion Loss (dB)	Center Frequency (GHz)	Absorption Rate (%)	Center Frequency (GHz)		
Ref. [24]	1.2	8.61 and 11.33	92	10	Surface	Single
Ref. [25]	1.96	4	90	5.2	Drilling	Double
Ref. [33]	0.97	0–0.8	90	8–18	Drilling	Double
This work	0.85	11.4 GHz	92	11.4 GHz	Surface	Single

The asymmetry of the structure can be compensated to achieve the conversion between absorption and transmission modes by adjusting the bias voltage of the varactors. The measurement results are shown in Figure 9 under the oblique incidence of 0–30°. The solid line represents the return loss and the dashed line denotes the insertion loss. When the bias voltage is changed at different incident angles, the transmission performance is relatively stable, but the absorption behavior is slightly worse. Therefore, the angular response of the asymmetric structures by changing the surface impedance of the proposed design is somewhat limited.

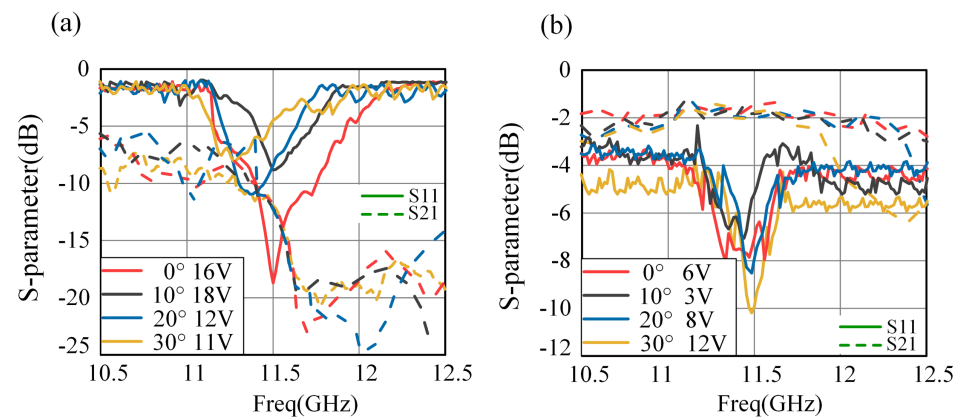


Figure 9. Measurement results for different incidences in TE polarization of the proposed AFSS: (a,b) are the scattering parameters of absorption and transmission states, respectively.

5. Conclusions

A compact AFSS that can switch between absorption and transmission modes in the same frequency by controlling the lumped components on the AFSS is proposed in this paper. The reconfigurable AFSS structure is designed, analyzed, and measured, whereas it not only realizes the dual-functional conversion between transmission and absorption modes at the same frequency but also compensates the angular sensitivity of the asymmetric structures by independently controlling the bias conditions (ON-/OFF-state) of the PIN diodes and the tuning capacitance value of the varactors. Both equivalent circuit modeling and surface current analysis are used to further analyze the absorption and transmission mechanism of the designed structure, which outstands the functionality of the active components in mode conversion. The designed AFSS was manufactured by PCB technology and measured in an anechoic chamber. Both simulated and measured results demonstrate that the presented structure has the capability to achieve transmission/absorption conversion in the same frequency of around 11.4 GHz under normal incidence. The absorption and transmission modes are angularly stable up to 35° by changing the capacitance of the varactors, which compensates for the asymmetry of the structure. The proposed AFSS is of high value in applications scenarios that are not sensitive to polarization, such as antenna dome, etc.

Author Contributions: Conceptualization, T.D. and C.-Z.H.; methodology, C.-Z.H.; software, Y.L.; validation, Y.L. and W.W.; formal analysis, Y.L. and W.W.; investigation, W.W.; writing—original draft preparation, Y.L.; writing—review and editing, T.D.; supervision, C.-Z.H.; project administration, T.D.; funding acquisition, T.D. and C.-Z.H. All authors have read and agreed to the published version of the manuscript.

Funding: This research was funded by the Natural Science Foundation of Fujian Province under grant number 2022J01342 and 2021J05178.

Data Availability Statement: Please contact the corresponding authors for the data.

Conflicts of Interest: The authors declare no conflict of interest.

References

1. Landy, N.I.; Sajuyigbe, S.; Mock, J.J.; Smith, D.R.; Padilla, W.J. Perfect metamaterial absorber. *Phys. Rev. Lett.* **2008**, *100*, 207402. [[CrossRef](#)] [[PubMed](#)]
2. Munk, B.A. *Frequency Selective Surfaces: Theory and Design*; Wiley: New York, NY, USA, 2005.
3. Mias, C. Varactor tunable frequency selective absorber. *Electron. Lett.* **2003**, *39*, 1060–1062. [[CrossRef](#)]
4. Xu, W.R.; Sonkusale, S. Microwave diode switchable metamaterial reflector/absorber. *Appl. Phys. Lett.* **2013**, *103*, 031902. [[CrossRef](#)]
5. Tennant, A.; Chambers, B. A single-layer tunable microwave absorber using an active FSS. *IEEE Microwave. Wirel. Compon. Lett.* **2004**, *14*, 46–47. [[CrossRef](#)]

6. Kontt, E.F.; Schaeffer, J.F.; Tuley, M.T. *Radar Cross Section: Its Prediction Measurement and Reduction*; Artech House: Boston, MA, USA, 1985.
7. Li, F.F.; Fang, W.; Chen, P.; Poo, Y.; Wu, R.X. Transmission and radar cross-section reduction by combining binary coding metasurface and frequency selective surface. *Opt. Express* **2018**, *26*, 33878. [[CrossRef](#)]
8. Xu, B.; Gu, C.; Li, Z.; Liu, L.; Niu, Z. A novel absorber with tunable bandwidth based on graphene. *IEEE Antennas Wirel. Propag. Lett.* **2014**, *13*, 822–825.
9. Torabi, E.S.; Fallahi, A.; Yahaghi, A. Evolutionary optimization of graphene-metal metasurfaces for tunable broadband terahertz absorption. *IEEE Trans. Antennas Propag.* **2017**, *65*, 1464–1467. [[CrossRef](#)]
10. Ho, I.C.; Pan, C.L.; Hsieh, C.F.; Pan, R.P. Liquid-crystal-based terahertz tunable Solc filter. *Opt. Lett.* **2006**, *88*, 910. [[CrossRef](#)]
11. Hu, W.; Dickie, R.; Cahill, R.; Gamble, H.; Ismail, Y.; Fusco, V.; Linton, D.; Grant, N.; Rea, S. Liquid crystal tunable mm wave frequency selective surface. *IEEE Microw. Wirel. Components Lett.* **2007**, *17*, 667–669. [[CrossRef](#)]
12. Deng, G.; Xia, T.; Jing, S.; Yang, J.; Lu, H.; Yin, Z. A tunable metamaterial absorber based on liquid crystal intended for F frequency band. *IEEE Antennas Wirel. Propag. Lett.* **2017**, *16*, 2062–2065. [[CrossRef](#)]
13. Mias, C. Varactor-tunable frequency selective surface with resistive-lumped-element biasing grids. *IEEE Microw. Wirel. Components Lett.* **2005**, *15*, 570–572. [[CrossRef](#)]
14. Li, J.; Jiang, J.; He, Y.; Xu, W.; Chen, M.; Miao, L.; Bie, S. Design of a tunable low-frequency and broadband radar absorber based on active frequency selective surface. *IEEE Antennas Wirel. Propag. Lett.* **2016**, *15*, 774–777. [[CrossRef](#)]
15. Zhou, Z.; Chen, K.; Zhu, B.; Zhao, J.; Feng, Y.; Li, Y. Ultra-Wideband Microwave Absorption by Design and Optimization of Metasurface Salisbury Screen. *IEEE Access* **2018**, *6*, 26843–26853. [[CrossRef](#)]
16. Ji, C.; Huang, C.; Zhang, X.; Yang, J.; Song, J.; Luo, X. Broadband low-scattering metasurface using a combination of phase cancellation and absorption mechanisms. *Opt. Express* **2019**, *27*, 23368. [[CrossRef](#)]
17. Hoa, N.T.Q.; Tuan, T.S.; Hieu, L.T.; Giang, B.L. Facile design of an ultra-thin broadband metamaterial absorber for C-band applications. *Sci. Rep.* **2019**, *9*, 468. [[CrossRef](#)]
18. Zhu, B.; Feng, Y.; Zhao, J.; Huang, C.; Wang, Z.; Jiang, T. Polarization modulation by tunable electromagnetic metamaterial reflector/absorber. *Opt. Express* **2010**, *18*, 23196–23203. [[CrossRef](#)]
19. Chen, L.; Qu, S.; Chen, B.; Bai, X.; Ng, K.; Chan, C.H. Terahertz Metasurfaces for Absorber or Reflectarray Applications. *IEEE Trans. Antennas Propag.* **2017**, *65*, 234–241. [[CrossRef](#)]
20. Yoo, M.; Lim, S. Active metasurface for controlling reflection and absorption properties. *Appl. Phys. Express* **2014**, *7*, 112204. [[CrossRef](#)]
21. Zhang, X.; Wei, Z.; Fan, Y.; Wu, C.; Cheng, K.; Qi, L.; Zhang, B.; Zhang, X. Ultrathin dual-functional metasurface with transmission and absorption characteristics. *Opt. Mater. Express* **2018**, *8*, 875. [[CrossRef](#)]
22. Pang, Y.; Li, Y.; Qu, B.; Yan, M.; Wang, J.; Qu, S.; Xu, Z. Wideband RCS reduction metasurface with a transmission window. *IEEE Trans. Antennas Propag.* **2020**, *68*, 7079–7087. [[CrossRef](#)]
23. Zhao, H.Z.; Zhou, Y.J. A Tunable Absorber with Switched Absorption/Transmission Property. In Proceedings of the 2018 Cross Strait Quad-Regional Radio Science and Wireless Technology Conference (CSQRWC), Xuzhou, China, 21–24 July 2018; pp. 1–3.
24. Phon, R.; Ghosh, S.; Lim, S. Novel multifunctional reconfigurable active frequency selective surface. *IEEE Trans. Antennas Propag.* **2018**, *67*, 1709–1718. [[CrossRef](#)]
25. Phon, R.; Ghosh, S.; Lim, S. Active frequency selective surface to switch between absorption and transmission band with additional frequency tuning capability. *IEEE Trans. Antennas Propag.* **2019**, *67*, 6059–6067. [[CrossRef](#)]
26. Yu, Y.; Xiao, F.; He, C.; Jin, R.; Zhu, W. Double-arrow metasurface for dual-band and dual-mode polarization conversion. *Opt. Express* **2020**, *28*, 11797–11805. [[CrossRef](#)]
27. Pan, Y.; Lan, F.; Zhang, Y.; Zeng, H.; Wang, L.; He, T.S.G.; Yang, Z. Dual-band multifunctional coding metasurface with a mingled anisotropic aperture for polarized manipulation in full space. *Photonics Res.* **2022**, *10*, 416–425. [[CrossRef](#)]
28. Silalahi, H.; Chiang, W.; Shih, Y.; Wei, W.; Su, J.; Huang, C. Folding metamaterials with extremely strong electromagnetic resonance. *Photonics Res.* **2022**, *10*, 2215–2222. [[CrossRef](#)]
29. Oman, Z.; Ghobadi, A.; Khalichi, B.; Ozbay, E. Fano resonance in a dolomite phase-change multilayer design for dynamically tunable omnidirectional monochromatic thermal emission. *Opt. Lett.* **2022**, *47*, 5781–5784. [[CrossRef](#)]
30. Zhao, F.; Li, Z.; Li, S.; Dai, X.; Zhou, Y.; Liao, X.; Cao, J.C.; Liang, G.; Shang, Z.; Zhang, Z.; et al. Terahertz metalens of hyper-dispersion. *Photonics Res.* **2022**, *10*, 886–895. [[CrossRef](#)]
31. Liu, S.; Xu, F.; Zhan, J.; Qiang, J.; Xie, Q.; Yang, L.; Deng, S.; Zhang, Y. Terahertz liquid crystal programmable metasurface based on resonance switching. *Opt. Lett.* **2022**, *47*, 1891–1894. [[CrossRef](#)]
32. Silalahi, H.; Shih, Y.; Lin, S.; Chen, Y.; Wei, W.; Chao, P.; Huang, C. Electrically controllable terahertz metamaterials with large tunabilities and low operating electric fields using electrowetting-on-dielectric cells. *Opt. Lett.* **2021**, *46*, 5962–5965. [[CrossRef](#)] [[PubMed](#)]
33. Hu, Z.; Chen, Y.; Xiao, S. Design of Metasurface with Low-Frequency Transmission and High-Frequency Absorption Characteristics. In Proceedings of the 2020 IEEE International Conference on Computational Electromagnetics (ICCEM), Singapore, 24–26 August 2020; pp. 226–227. [[CrossRef](#)]
34. Kaynak, A.; Unsworth, J.; Clout, R.; Mohan, A.S.; Beard, G.E. A study of microwave transmission, reflection, absorption, and shielding effectiveness of conducting polypyrrole films. *J. Appl. Polym.* **2010**, *54*, 269–278. [[CrossRef](#)]

35. Azad, A.K.; Taylor, A.J.; Smirnova, E.I.; Ohara, J.F. Characterization and analysis of terahertz metamaterials based on rectangular split-ring resonators. *Appl. Phys. Lett.* **2008**, *2*, 011119. [[CrossRef](#)]
36. Fu, L.; Schweizer, H.; Guo, H.; Liu, N.; Giessen, H. Synthesis of transmission line models for metamaterial slabs at optical frequencies. *Phys. Rev.* **2008**, *78*, 115110. [[CrossRef](#)]
37. Caloz, C. *Electromagnetic Metamaterials: Transmission Line Theory and Microwave Applications: The Engineering Approach*; John Wiley and Sons: New York, NY, USA, 2005.
38. Frickey, D.A. Conversions between S, Z, Y, H, ABCD, and T parameters which are valid for complex source and load impedances. *IEEE Trans. Microw. Theory Tech.* **1994**, *42*, 205–211. [[CrossRef](#)]
39. Zhao, J.; Cheng, Q.; Chen, J.; Qi, M.Q.; Jiang, W.X.; Cui, T.J. A tunable metamaterial absorber using varactor diodes. *New J. Phys.* **2013**, *15*, 043049. [[CrossRef](#)]
40. Shang, Y.; Shen, Z.; Xiao, S. On the design of single-layer circuit analog absorber using double-square-loop array. *IEEE Trans. Antennas Propag.* **2013**, *61*, 6022–6029. [[CrossRef](#)]

Disclaimer/Publisher’s Note: The statements, opinions and data contained in all publications are solely those of the individual author(s) and contributor(s) and not of MDPI and/or the editor(s). MDPI and/or the editor(s) disclaim responsibility for any injury to people or property resulting from any ideas, methods, instructions or products referred to in the content.